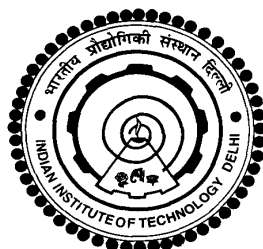


**SUPERCONDUCTING AND MAGNETIC PROPERTIES
OF NEW LAYERED METAL PnictIDES AND
CHALCOGENIDES**

GOHIL S. THAKUR



**DEPARTMENT OF CHEMISTRY
INDIAN INSTITUTE OF TECHNOLOGY DELHI
MAY 2016**

©Indian Institute of Technology Delhi (IITD), New Delhi, 2016

**SUPERCONDUCTING AND MAGNETIC PROPERTIES
OF NEW LAYERED METAL PnictIDES AND
CHALCOGENIDES**

by

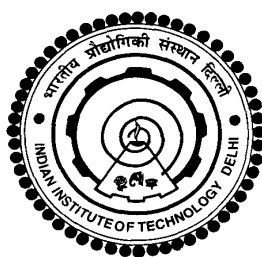
GOHIL S. THAKUR

Department of Chemistry

Submitted

in fulfillment of the requirement of the Degree of Doctor of Philosophy

to the



INDIAN INSTITUTE OF TECHNOLOGY DELHI

MAY 2016

DEDICATED TO MY
FAMILY

CERTIFICATE

This is to certify that the thesis entitled, “Superconducting and magnetic properties of new layered metal pnictides and chalcogenides”, being submitted by **Mr. Gohil S. Thakur**, to the Indian Institute of Technology, Delhi for the award of the degree of Doctor of Philosophy in Chemistry, is a record of bonafide research work carried out by him. Mr. Gohil S. Thakur has worked under my guidance and supervision, and has fulfilled the requirements for the submission of this thesis, which to my knowledge has reached the requisite standard.

The results contained in this dissertation have not been submitted in part or full, to any other university or institute for award of any degree or diploma.

Date:

Professor A. K. Ganguli

Department of Chemistry

Indian Institute of Technology, Delhi

New Delhi – 110016.

INDIA

ACKNOWLEDGMENTS

*This thesis, and the research it is based on, would not have been possible without the help of many people. Foremost, I am deeply indebted to my supervisor, **Prof. Ashok Kumar Ganguli**, for introducing me to the most fascinating field of superconductivity. I thank him for the efforts he has made to groom me as a researcher since the day I joined him as a research student. I am amazed by the enthusiasm that he has towards science and his presence has motivated me to love science. I thank him for his guidance, support, critical suggestions and for everything he taught me during the past six years. He has been a source of inspiration for me and my labmates.*

*I am indebted to a special person, **Prof L. C. Gupta** (Visiting scientist at the Dept of Chemistry, IIT Delhi and retd. Professor at TIFR Mumbai) without whom this work would not have been possible. I thank him for helping and motivating me throughout my research career, for all those numerous scientific discussions that I had with him which led to fruitful results. He taught me how to perceive a problem scientifically.*

I am also grateful to the Head, Prof Ravi Shankar and former Head's Prof A. K. Singh and Prof. A. Ramanan, Department of Chemistry, IIT Delhi for providing the necessary facilities in the department. I am grateful to all supporting staff at the department, IIT Delhi for their kind help and cooperation. I also thank Dr. Pramit Chaudhury for extending his help in the absence of my supervisor.

The work in this thesis is a result of joint collaborative effort of various groups across and outside the country. I am extremely thankful to Prof. Jeffery Lynn and Dr. Yang Zhao (NIST Center for Neutron Research, Maryland, USA) for carrying out neutron diffraction measurement on my CuFeAs and LnCuAs₂ samples and for all the useful guidance and discussions. I am also very thankful to our collaborators Prof. G. Fuchs, Prof. K. Nenkov and Prof. V. Grinenko (IFW, Dresden) for carrying out Transport, magnetic and specific heat measurements on SrFBiS₂ samples. I thank Prof V. P. S. Awana and Mr. Rajveer Jha (NPL, New Delhi) for carrier high pressure transport measurements on EuFBiS₂ and CeOBiS₂ samples. I also thank Prof. S. Arumugam, Dr.

Kanagraj and Mr. Kalaiselvan for carrying out transport and magnetic measurements on various materials. I am thankful to my collaborators Prof. S. Patnaik, Mr Vishal Mourya, Mrs. Shruti and Ms. Prakriti Neha (JNU, New Delhi) for performing transport and magnetic properties measurement. I also thank Dr. Goutam Sheet and his team at IISER Mohali, for a fruitful collaboration.

I wish to express my gratitude for my seniors and colleagues, Dr. Saroj, Dr. Jahangeer, Dr. Sonalika, Dr. Aparna Dr. Menaka, Dr. Masood, Dr. Jaiprakash, Dr. Aditya, Dr. Parthsarthy, Dr. Debashree, Dr. Sunita, Dr. Soma, Dr. Sharmila, Neha, Nibedita, Zeba, Nitin, Vaishali, for making the lab environment cordial and for helping me whenever required.

I am really grateful to my labmates and friends Dr. Mrinmoyee, Dr. Surojit, Dr. Bharat, Soumen, Sandeep, Arabinda, Kasinath, Sanjit, Pintu and Vandana for their great support both professionally and personally and for making my stay at IIT Delhi fun and memorable.

Thanks to my friends specially Kushagra, Nagendra and Praveen for being there whenever I needed their help.

I owe everything to my parents Mr. J. K. Thakur and Mrs. Suman Thakur and my sisters Mrs. Sonal and Sheetal. They made me what I am. Without their support and encouragement I would not have moved a step ahead. I cannot thank them enough for all the sacrifices that they made, all the discomfort they bore for comforting me. I found them always standing by my side supporting my decisions and loving and caring unconditionally. They have been a constant source of encouragement, inspiration and strength. They taught me the importance of being disciplined in life and to take the right decisions at the right time. I thank all my family near and far

I would take this opportunity to thank my wife and great friend Anjali for being a constant pillar of support and for her unconditional love, care moral support and delicious food! I thank her for being there in all my thick and thin.

I also thank our football team the AAFC gang for all the fun and joy we had during the play. Thanks for making my PhD less boring and more fun.

I am sincerely thankful to all those who have helped me in the successful completion of this work.

I acknowledge the financial support of Department of Science and Technology (DST) and Council of Scientific and Industrial Research (CSIR) Govt. of India for fellowships.

Gohil S Thakur

Abstract

Mankind is always intrigued by new materials and unusual properties. Constant efforts are made to understand the unusual properties within the framework of existing theories. Superconductivity is one such property of matter that has fascinated the researchers for over a century. Significant research activity in the broad area of superconductivity has led to many exciting discoveries in the past like the superconductivity in metals, alloys, heavy-fermion superconductors, high T_c oxide superconductors and even superconductivity in magnetic materials. After the euphoria of high T_c oxide superconductors, Fe-based layered pnictide and rare-earth based chalcogenides have garnered special attention due to immense scope of further exploration. In this work we present our efforts to investigate new superconducting materials related to LnOBiS₂ and AFBiS₂ family. Apart from these novel layered magnetic materials of the type CuFePn (Pn = As and Sb) with Cu₂Sb structure were synthesized and studied. Magnetic structure of rare-earth based layered pnictide LnCuAs₂ (with ZrCuSi₂ type structure) has been studied using neutron diffraction technique. All the compounds studied crystallize in $P4/nmm$ space group. There are several hundreds of known materials of these two classes with interesting properties like magnetism and superconductivity. Hence, there exists a huge possibility of manipulating electronic, magnetic and other properties by chemical substitution at various sites leading to tailor made materials.

Effects of isovalent chemical substitution on the superconducting and magnetic properties of LnO_{0.5}F_{0.5}BiS₂ have been investigated. Structural studies have been carried out in detail. Substitution of smaller Sm ion at La site in LaO_{0.5}F_{0.5}BiS₂ (La_{1-y}Sm_yO_{0.5}F_{0.5}BiS₂; $y = 0.0$ to

1.0) leads to an enhancement in T_c from 2.5 K for $y = 0.0$ to 4.6 K for $y = 0.8$. This enhancement in T_c is related to the structural distortion in Bi–S layers which is caused by increased chemical pressure. Single crystal of the new member of this class $\text{SmO}_{0.5}\text{F}_{0.5}\text{BiS}_2$ ($y = 1.0$) is surprisingly found to be non–superconducting. Y substitution on Ce sites ($\text{Ce}_{1-x}\text{Y}_x\text{O}_{0.5}\text{F}_{0.5}\text{BiS}_2$; $x = 0.0$ – 0.3) leads to a small enhancement in the T_c (from $T_c = 2.4$ K for $x = 0$ to $T_c = 3$ K for $x = 0.2$). This material also shows coexistence of superconductivity and ferromagnetism.

We have studied Se substituted $\text{Sr}_{0.5}\text{Ce}_{0.5}\text{FBiS}_{2-x}\text{Se}_x$ ($x = 0, 0.5$ and 1.0) and La substituted $\text{Eu}_{1-x}\text{La}_x\text{FBiS}_2$ ($x = 0, 0.5$ and 0.6). $\text{Sr}_{0.5}\text{Ce}_{0.5}\text{FBiS}_2$ exhibits coexistence of superconductivity and ferromagnetism ($T_c = 2.5$ K and $T_C = 7.5$ K). Se substitution at S sites induces bulk superconductivity with enhanced T_c upto 3.3 K. Sharp diamagnetic signal in susceptibility is observed which was not observed in sample with $x = 0$ (Se free). We observed unique *dual magnetic hysteresis loops* with superposition of ferromagnetic and superconducting loops indicating clear coexistence of superconductivity and magnetism in Se doped samples. This kind of hysteresis loop is a novel feature and has been observed for the first time in Bi–S₂ superconductors. A marked reduction in Ce moment ($\sim 0.1 \mu_B$) in the superconducting state suggests itinerant ferromagnetism. Enhancement of T_c from 0.3 K (in EuFBiS_2) to 2.5 K is observed in $\text{Eu}_{1-x}\text{La}_x\text{BiS}_2\text{F}$ ($x = 0.5$ and 0.6). Upon application of pressure (upto 2.5 GPa) on $x = 0.5$ composition, further enhancement in T_c (upto 10 K) is observed. We speculate that this material undergoes a structural phase transition under high pressure. This is the first case where such a great enhancement (~ 30 folds) in T_c has been observed.

Compositions of the type $\text{FeTe}_{0.5}\text{Se}_{0.5-x}\text{O}_x$ ($x = 0, 0.01, 0.03, 0.04$ and 0.06) and $\text{Fe}_{1-x}\text{Mn}_x\text{Te}_{0.5}\text{Se}_{0.5}$ ($x = 0.01$ and 0.02) were also studied in detail. Partial O–substitution at Se sites leads to decrease in T_c from 14.9 to 13.1 (for $x = 0$ to $x = 0.06$, respectively). Also the diamagnetic signal becomes broad on increasing oxygen content. This decrease in T_c is attributed to the disorder created at Se/Te sites by substitution of oxygen which disturbs the Se/Te arrangement. Mn–doping (at Fe sites) also leads to a similar decrease in T_c . This is due to the pair–breaking effect of Mn^{2+} –ions.

We have synthesized some new phases CuFePn ($\text{Pn} = \text{As}$ and Sb) belonging to Cu_2Sb family which structurally resemble the superconducting LiFeAs . CuFeSb is found to be room temperature soft–ferromagnet with Curie temperature $T_C \sim 375$ K with Fe moment $\sim 1.8\mu_B$ in the ordered state. On the other hand CuFeAs was found to be weak antiferromagnetic with $T_N \sim 9$ K and a very small Fe moment of $\sim 0.1 \mu_B$. Magnetic properties of these phases are confirmed by variable temperature Mössbauer studies. The anion height plays an important in deciding the magnetic ground state of these Fe–pnictides.

Magnetic structures of layered arsenide LnCuAs_2 ($\text{Ln} = \text{Pr}, \text{Nd}, \text{Tb}, \text{Dy}, \text{Ho}$ and Yb) have been determined. All these phases show antiferromagnetic ordering at low temperature (2–13 K). PrCuAs_2 and NdCuAs_2 were found to have a simple commensurate structure below T_N (6.4 and 3.5 K respectively) with propagation vector $k = (0, 0, 0.5)$. While the Pr moments align along the crystallographic c –axis, Nd and Dy moments lie in the ab –plane. The difference in the moment alignment is attributed to the crystal field effects. TbCuAs_2 and HoCuAs_2 exhibit a complex *incommensurate* magnetic structure below T_N

TABLE OF CONTENTS

CERTIFICATE		i
ACKNOWLEDGEMENTS		ii
ABSTRACT		v
TABLE OF CONTENTS		viii
LIST OF FIGURES		xiii
LIST OF TABLES		xxviii
ABBREVIATIONS AND SYMBOLS		xxxii
Chapter 1:	Introduction	
1.1	Important properties of superconductors	3
1.1.1	Meissner Effect	5
1.1.2	Penetration depth	6
1.2	The BCS theory	7
1.3	Type I and Type II superconductors	9
1.4	Critical current density (J_c)	12
1.5	Brief history of superconducting materials	12
1.6	Crystal structure of new layered pnictide and chalcogenide superconductors	16
1.7	Electronic structures of recently discovered layered superconductors	27

1.8	Electrical and magnetic properties of recently discovered layered pnictides and chalcogenides	33
1.8.1	Electrical properties	33
1.8.2	Magnetic properties	37
1.9	Synthesis Techniques	42
1.9.1	Sealed tube method (solid state method)	42
1.9.2	Molten salt method	43
1.9.3	High pressure method	44
1.10	Characterization Techniques	44
1.10.1	Powder X-ray and neutron diffraction	44
1.10.2	Scanning electron microscopy (SEM)	50
1.11	Motivation of the thesis.	51

Chapter 2: Superconductivity in doped $\text{LnO}_{1-x}\text{F}_x\text{BiS}_2$ (Ln = La, Ce and Sm)

2.1	Introduction	68
2.2	Experimental	72
2.2.1	Materials and synthesis	72
2.2.2	Characterization	73
2.2.3	Resistivity measurement	74
2.2.4	Magnetic Measurement	74
2.3	Results and Discussion	75
2.3.1	Structural and compositional analysis	75
2.3.2	Resistivity and magnetic measurements	89

2.4	References	102
-----	------------	-----

Chapter 3: Superconductivity in doped AFBiS_2 compounds (A = Sr and Eu):

$\text{Sr}_{0.5}\text{Ce}_{0.5}\text{FBiS}_{2-x}\text{Se}_x$ and $\text{Eu}_{1-x}\text{La}_x\text{FBiS}_2$

3.1	Introduction	112
3.2	Experimental	116
3.2.1	Materials and synthesis	116
3.2.2	Characterization	117
3.2.3	Resistivity Measurement	118
3.2.4	Magnetic Measurement	118
3.2.5	Specific heat	118
3.3	Results and Discussion	119
3.3.1	Structure and compositional analysis	119
3.3.2	Resistivity and Magnetic studies	125
3.4	References	145

Chapter 4: Effect of O- and Mn- doping on superconductivity in $\text{FeTe}_{0.5}\text{Se}_{0.5}$

superconductor

4.1	Introduction	153
4.2	Experimental	157
4.2.1	Materials and synthesis	156
4.2.2	Characterization	157
4.2.3	Resistivity Measurements	158

4.2.4	Magnetic Measurement	158
4.3	Results and Discussion	158
4.3.1	Structural and compositional analysis	159
4.3.2	Resistivity and magnetic studies	168
4.4	References	175

Chapter 5: Synthesis and properties of CuFePn (Pn = As and Sb): New members of Cu₂Sb family

5.1	Introduction	182
5.2	Experimental	184
5.2.1	Materials and synthesis	184
5.2.2	Characterization	185
5.2.3	Resistivity Measurement	186
5.2.4	Magnetic Measurement	186
5.2.5	Neutron diffraction	187
5.2.6	⁵⁷ Fe Mössbauer spectroscopy	187
5.3	Results and Discussion	188
5.3.1	Phase analysis and structure determination	188
5.3.2	Magnetic and Resistivity studies	200
5.3.3	Mössbauer Studies	207
5.3.3.1	Zero field Mössbauer spectroscopy of CuFeAs	207
5.3.2.2	Transverse field Mössbauer spectroscopy of CuFeAs	210
5.3.2.3	Zero field ⁵⁷ Fe Mössbauer spectroscopy of CuFeSb	211

5.4	References	215
-----	------------	-----

Chapter 6: Magnetic structure determination of LnCuAs₂ (Ln = Pr, Nd, Tb, Dy, Ho and Yb)

6.1	Introduction	221
6.2	Experimental	223
6.2.1	Materials and synthesis	223
6.2.2	Characterization	223
6.2.3	Magnetic Measurements	224
6.2.4.	Neutron diffraction	224
6.3	Results and Discussion	225
6.3.1	Phase analysis and structure determination	225
6.3.2.	Magnetic studies	228
6.3.2.1.	Susceptibility studies	228
6.3.2.2.	Neutron diffraction studies	230
6.4	References	245

Chapter 7: Conclusions and scope for further research

7.1	Conclusion	249
7.2	Scope of future work	254

Bio-Data of the Author		257
-------------------------------	--	-----

LIST OF FIGURES

Figure No.	Figure Caption	Page No.
Figure 1.1	Variation of resistivity with temperature for $\text{Sr}_{0.5}\text{Ce}_{0.5}\text{FBiSSe}$ superconductor. Inset shows the diamagnetic transition below T_c	4
Figure 1.2	Magnetic flux expulsion from interior of a superconductor.	5
Figure 1.3	Penetration of magnetic field inside a superconductor	6
Figure 1.4	Specific heat for V_3Si in superconducting (circles) and normal state (diamonds)	8
Figure 1.5	Temperature dependence of H_c for type I superconductors	9
Figure 1.6	Temperature dependence of H_c for type II superconductors	10
Figure 1.7	T_c of some new superconducting compounds discovered after 2010.	16
Figure 1.8	Crystal structure of LaOFeAs (space group $P4/nmm$)	17
Figure 1.9	Coordination environments around (a) La and (b) Fe	18
Figure 1.10	Crystal structure of tetragonal FeSe [9] (space group $P4/nmm$).	20
Figure 1.11	Crystal structure of LiFeAs (space group $P4/nmm$)	22

Figure 1.12	Crystal structure of CeOBiS ₂ [53] (space group $P4/nmm$) and coordination around Bi.	24
Figure 1.13	Crystal structure of LnCuAs ₂ showing the coordination of different atoms.	26
Figure 1.14	Crystal structures of some layered arsenide and chalcogenides. The shaded portion denotes the conducting layers.	27
Figure 1.15	Density of states and Fermi surface of LaOFeAs	28
Figure 1.16	LDA Density of states and (b) Fermi surface for LiFeAs	29
Figure 1.17	LDA density of states (main panel) and Fermi surface (insets) for FeSe and FeTe	30
Figure 1.18	Density of states for LaO _{1-x} F _x BiS ₂ ; $x = 0$ (left) and $x = 0.5$ (right)	32
Figure 1.19	Fermi surface of LaO _{0.5} F _{0.5} BiS ₂	33
Figure 2.1	Crystal structure of LnOBiS ₂	69
Figure 2.2	Variation of T_c with F-content (x) in LnO _{1-x} F _x BiS ₂	70
Figure 2.3	Powder x-ray diffraction patterns for SmO _{1-x} F _x BiS ₂	76

- Figure 2.4** (a) Photograph of crystals of $\text{SmO}_{0.5}\text{F}_{0.5}\text{BiS}_2$ as seen on a millimeter grid. (b) Electron micrograph of a selected $\text{SmO}_{0.5}\text{F}_{0.5}\text{BiS}_2$ crystal with dimension $220\ \mu\text{m} \times 120\ \mu\text{m} \times 20\ \mu\text{m}$. 77
- Figure 2.5** SEM–EDAX spectrum of a selected $\text{SmO}_{0.5}\text{F}_{0.5}\text{BiS}_2$ crystal 77
- Figure 2.6** Rietveld refinement studies of powder x-ray diffraction pattern for $\text{SmO}_{0.5}\text{F}_{0.5}\text{BiS}_2$. Pink and green vertical bars indicate the allowed Bragg reflections for $\text{SmO}_{0.5}\text{F}_{0.5}\text{BiS}_2$ (90%) and Bi_2S_3 phases (~ 10 %) respectively. Blue line is the difference plot. Inset shows the fit in the high angle region. 78
- Figure 2.7** (a) Powder X-ray diffraction patterns for $\text{La}_{1-y}\text{Sm}_y\text{O}_{0.5}\text{F}_{0.5}\text{BiS}_2$ (b) and (c) variation of (200) and (004) peaks with Sm content (y) for $\text{La}_{1-y}\text{Sm}_y\text{O}_{0.5}\text{F}_{0.5}\text{BiS}_2$ signifying the systematic decrease in a -lattice parameter with Sm content. 82
- Figure 2.8** Rietveld refinement of powder X-ray diffraction patterns for $\text{La}_{1-y}\text{Sm}_y\text{O}_{0.5}\text{F}_{0.5}\text{BiS}_2$. Black (+) and red line corresponds to observed and calculated intensities. Vertical bars mark the allowed Bragg reflections for different phases. Blue line is the difference of observed and calculated intensities. 83
- Figure 2.9** Variation of in-plane S–Bi–S bond angles and Bi–S bond 86

length for $\text{La}_{1-y}\text{Sm}_y\text{O}_{0.5}\text{F}_{0.5}\text{BiS}_2$ with Sm content.

- Figure 2.10** (a) Powder XRD patterns of $\text{Ce}_{1-x}\text{Y}_x\text{O}_{0.5}\text{F}_{0.5}\text{BiS}_2$ (b) variation of cell volume (main panel) and lattice parameter a and c (inset) with yttrium content x . **88**
- Figure 2.11** Resistivity versus temperature plots at different magnetic fields (0–9T) for polycrystalline $\text{SmO}_{0.5}\text{F}_{0.5}\text{BiS}_2$ (main panel) and undoped SmOBiS_2 (inset). **89**
- Figure 2.12** Variable temperature susceptibility data for $\text{SmO}_{1-x}\text{F}_x\text{BiS}_2$ ($x = 0.0$ and 0.5) crystals measured in a field of 30 Oe (main panel). Inset shows inverse susceptibility plot with the Curie-Weiss fit (red line) for $\text{SmO}_{0.5}\text{F}_{0.5}\text{BiS}_2$ in the low temperature region **90**
- Figure 2.13** Isothermal magnetization plots at different temperatures (2, 50, 150 and 300 K) for $\text{SmO}_{0.5}\text{F}_{0.5}\text{BiS}_2$. **91**
- Figure 2.14** Temperature dependent resistivity normalized to its value at 10 K for $\text{La}_{1-y}\text{Sm}_y\text{O}_{0.5}\text{F}_{0.5}\text{BiS}_2$. Inset show the normalized resistivity in the full temperature range (2–300 K) **92**
- Figure 2.15** Variable temperature magnetization curves near superconducting transition for $\text{La}_{1-y}\text{Sm}_y\text{O}_{0.5}\text{F}_{0.5}\text{BiS}_2$. Inset shows the variation of T_c obtained from magnetization and resistivity measurements with Sm content **93**

- Figure 2.16** Temperature dependent resistivity plots with for $\text{Ce}_{1-x}\text{Y}_x\text{O}_{0.5}\text{F}_{0.5}\text{BiS}_2$ in the temperature range 2–300 K showing semiconducting like behavior till 5 K. Inset shows low temperature resistivity near the superconducting transition **95**
- Figure 2.17** Variation of $\rho_{300\text{K}}$, ρ_{max} and T_c plotted as a function of Y-doping (x) **96**
- Figure 2.18** (a) Field dependence of resistivity and (b) H_{c2} vs T plot with WHH fit (red line) for $\text{Ce}_{0.8}\text{Y}_{0.2}\text{O}_{0.5}\text{F}_{0.5}\text{BiS}_2$. **97**
- Figure 2.19** (a) Variable temperature and (b) isothermal magnetization curves for $\text{Ce}_{1-x}\text{Y}_x\text{O}_{0.5}\text{F}_{0.5}\text{BiS}_2$. **99**
- Figure 3.1** Crystal structure of SrFBiS_2 **113**
- Figure 3.2** T_c vs. pressure phase diagram for several rare-earth doped $\text{Sr}_{1-x}\text{Ln}_x\text{FBiS}_2$ materials **114**
- Figure 3.3** Powder X-ray diffraction patterns of $\text{Sr}_{0.5}\text{Ce}_{0.5}\text{FBiS}_{2-x}\text{Se}_x$ ($x = 0, 0.5$ and 1.0) **119**
- Figure 3.4** Energy dispersive analysis by X-ray (EDX) for $\text{Sr}_{0.5}\text{Ce}_{0.5}\text{FBiS}_2$ Se_x ($x = 0.5$ and 1.0). Insets show the electron micrographs of the samples and the selected regions on which the elemental **121**

analysis were performed

- Figure 3.5** Powder X-ray diffraction patterns of $\text{Eu}_{1-x}\text{La}_x\text{FBiS}_2$ ($x = 0.5$ and 0.6) collected at $T = 300$ K. 122
- Figure 3.6** Energy dispersive X-ray spectrum (EDX) of $\text{Eu}_{0.5}\text{La}_{0.5}\text{FBiS}_2$. 123
Inset shows the backscattered electron image of the sample on a $50 \mu\text{m}$ scale.
- Figure 3.7** Rietveld fit to the powder X-ray data for $\text{Eu}_{0.5}\text{La}_{0.5}\text{FBiS}_2$. 124
- Figure 3.8** Variable temperature resistivity plots for $\text{Sr}_{0.5}\text{Ce}_{0.5}\text{FBiS}_{2-x}\text{Se}_x$; $x = 0, 0.5$ and 1.0 (a) in temperature range $2-300$ K and (b) in low temperature range ($1 - 6$ K). Inset of (a) show the variation of T_c onset and T_c zero with Se doping. 125
- Figure 3.9** Upper critical field (H_{c2}) versus temperature (T) curve for $x = 0.5$ and 1.0 compositions (open circles) along with their WHH fit (solid lines). 127
- Figure 3.10** DC susceptibility curve in zero field cooled (ZFC) and field cooled (FC) conditions in low temperature range for $\text{Sr}_{0.5}\text{Ce}_{0.5}\text{FBiS}_2$. 129
- Figure 3.11** DC susceptibility curves in zero field cooled (ZFC) and field cooled (FC) conditions in low temperature range showing the onset of diamagnetic signal (arrow) for $\text{Sr}_{0.5}\text{Ce}_{0.5}\text{FBiS}_{1-x}\text{Se}_x$ ($x =$ 129

0.5 and 1.0).

- Figure 3.12** Plots of temperature dependent susceptibility and its derivative **130**
for $\text{Sr}_{0.5}\text{Ce}_{0.5}\text{FBiS}_{1-x}\text{Se}_x$ ($x = 0.5$ and 1.0)
- Figure 3.13** Magnetic and superconducting phase diagram of **131**
 $\text{Sr}_{0.5}\text{Ce}_{0.5}\text{FBiS}_{2-x}\text{Se}_x$.
- Figure 3.14** Temperature dependent paramagnetic susceptibility and its **132**
inverse for $\text{Sr}_{0.5}\text{Ce}_{0.5}\text{FBiS}_{2-x}\text{Se}_x$ ($x = 0.5$ and 1.0). Red line is the
Curie–Weiss fit.
- Figure 3.15** Isothermal magnetization loop for $\text{Sr}_{0.5}\text{Ce}_{0.5}\text{FBiS}_2$ at 2.5 K **133**
- Figure 3.16** Isothermal magnetization loops for Se doped samples **134**
 $\text{Sr}_{0.5}\text{Ce}_{0.5}\text{FBiS}_{2-x}\text{Se}_x$; $x = 0.5$ and 1.0 (**a** and **b**) in high field
range and (**c** and **d**) in low field range. Inset shows the initial
diamagnetic response.
- Figure 3.17** Temperature dependence of specific heat for **136**
 $\text{Sr}_{0.5}\text{Ce}_{0.5}\text{FBiS}_{1.5}\text{Se}_{0.5}$ measured at several applied magnetic
field. The increase of the specific heat at low temperatures
indicates a Schottky contribution.
- Figure 3.18** C/T vs. T^2 for $\text{Sr}_{0.5}\text{Ce}_{0.5}\text{FBiS}_{1.5}\text{Se}_{0.5}$ at $H = 0$ and low T (blue **138**
line). Red line: C/T data after subtraction of a Schottky
contribution which was approximated by the dashed line. (**b**)

Corrected C/T data vs. T^2 showing a linear behavior between 7–14 K

- Figure 3.19** (a) Variable temperature resistivity plots for $\text{Eu}_{1-x}\text{La}_x\text{BiS}_2\text{F}$ at ambient pressure in the temperature range 2–300 K range. Inset shows the resistivity in the low temperature range. (b) Pressure dependent resistivity plots for $\text{Eu}_{0.5}\text{La}_{0.5}\text{BiS}_2\text{F}$. (c) Magnified resistivity plots for $\text{Eu}_{0.5}\text{La}_{0.5}\text{BiS}_2\text{F}$ at different applied pressures in low temperature range. The violet lines show the criterion on selection of T_c . Arrow indicates the origin of kink in resistivity. **139**
- Figure 3.20** Plot of $\rho_{300\text{K}}$ and RRR with pressure for $\text{Eu}_{0.5}\text{La}_{0.5}\text{BiS}_2\text{F}$ **141**
- Figure 3.21** Pressure vs. T_c phase diagram for $\text{Eu}_{0.5}\text{La}_{0.5}\text{BiS}_2\text{F}$ showing regions with different T_c 's. **142**
- Figure 3.22** (a) Magnetic field dependent resistivity plot for $\text{Eu}_{0.5}\text{La}_{0.5}\text{BiS}_2\text{F}$ at an applied pressure of 2.5 GPa. (b) $H_{c2}(T)$ curves for $\text{Eu}_{0.5}\text{La}_{0.5}\text{BiS}_2\text{F}$ at $P = 2.5$ GPa; black squares are the experimental data points and red line is the WHH fit. **143**
- Figure 4.1** Crystal structure of FeSe consisting of edge shared FeSe tetrahedra. Here ' h ' is the anion height from the Fe plane. Open circle indicates the interstitial iron sites. **153**

- Figure 4.2** Magnetic and superconducting phase diagrams showing T_c , T_N 155
as a function of Se content (x) for (a) as-grown $\text{FeTe}_{1-x}\text{Se}_x$ and
(b) O_2 -annealed $\text{FeTe}_{1-x}\text{Se}_x$
- Figure 4.3** Powder X-ray diffraction patterns of $\text{FeTe}_{0.5}\text{Se}_{0.5-x}\text{O}_x$. Vertical 159
bars indicate the allowed Bragg reflections for $\text{FeTe}_{0.5}\text{Se}_{0.5}$.
- Figure 4.4** Variation of lattice parameters a and c as a function of oxygen 160
concentration (x).
- Figure 4.5** SEM-EDAX spectrum for nominal $\text{FeTe}_{0.5}\text{Se}_{0.44}\text{O}_{0.06}$ 161
composition showing the presence of elements Fe, Te and Se.
Inset shows the SEM micrograph of the same sample and the
regions on which the data were collected.
- Figure 4.6** Rietveld refinement plots for $\text{FeTe}_{0.5}\text{Se}_{0.5-x}\text{O}_x$ ($x = 0.0, 0.04,$ 162
 0.06).
- Figure 4.7** X-ray diffraction patterns for $\text{Fe}_{1-x}\text{Mn}_x\text{Te}_{0.5}\text{Se}_{0.5}$ ($x = 0, 0.01,$ 164
 0.02).
- Figure 4.8** EDAX analysis for $\text{Fe}_{0.98}\text{Mn}_{0.02}\text{Te}_{0.5}\text{Se}_{0.5}$ showing the presence 166
of elements Fe, Mn, Te and Se.
- Figure 4.9** Electron micrograph of a grain of $\text{Fe}_{0.98}\text{Mn}_{0.02}\text{Te}_{0.5}\text{Se}_{0.5}$ (left). 166
EDAX mapping showing the homogenous distribution of all the

elements in the selected grain (right).

- Figure 4.10** Rietveld refinement plot for $\text{Fe}_{0.98}\text{Mn}_{0.2}\text{Te}_{0.5}\text{Se}_{0.5}$. Vertical bars at the bottom represent allowed Bragg's reflections **167**
- Figure 4.11** Resistivity plots for $\text{FeTe}_{0.5}\text{Se}_{0.5-x}\text{O}_x$ ($x = 0.0, 0.01, 0.03, 0.04$ and 0.06). Inset shows the criterion of selection of T_c . **169**
- Figure 4.12** Variable temperature susceptibility for $\text{FeTe}_{0.5}\text{Se}_{0.5-x}\text{O}_x$ ($x = 0.0, 0.01, 0.03, 0.04$ and 0.06). Arrow marks the onset of superconductivity. **170**
- Figure 4.13** Variation of onset T_c with oxygen content 'x' obtained from magnetization and resistivity measurement. **170**
- Figure 4.14** Variable temperature resistivity plots for $\text{Fe}_{1-x}\text{Mn}_x\text{Te}_{0.5}\text{Se}_{0.5}$. **172**
- Figure 4.15** Variable temperature magnetization plots for $\text{Fe}_{1-x}\text{Mn}_x\text{Te}_{0.5}\text{Se}_{0.5}$ **172**
- Figure 5.1** Crystal structure of Cu_2Sb , showing the two copper sites. **183**
- Figure 5.2** Powder X-ray diffraction pattern of CuFeAs obtained after heating at different temperatures. **189**
- Figure 5.3** Energy dispersive X-ray (EDX) spectrum for CuFeAs . Image in the inset shows few regions where data were collected **191**
- Figure 5.4** Backscattered electron image of different regions of CuFeAs sample **192**

Figure 5.5	Rietveld fit to the powder X-ray diffraction data collected at 300 K for CuFeAs	192
Figure 5.6	Crystal structure of CuFeAs	194
Figure 5.7	Neutron powder diffraction data and its Rietveld fit for CuFeAs at 20 K. Arrow marks show the reflections corresponding to Cu ₃ As. (*) marks the unidentified impurity peaks	196
Figure 5.8	Powder X-ray diffraction pattern of CuFeSb obtained by reacting different combination of reactants, namely (a) Cu + Fe + Sb (b) Cu + FeSb (c) Cu ₂ Sb + Fe + Sb.	198
Figure 5.9	Rietveld fit to the powder X-ray diffraction data for CuFeSb.	199
Figure 5.10	Variable temperature magnetization data for CuFeAs at various applied magnetic fields in FC (closed symbols) and ZFC (open symbols) condition. (Inset) Magnetization data at H = 100 G.	201
Figure 5.11	Magnetic hysteresis loops for CuFeAs at various temperatures. Inset show the full hysteresis upto $H = \pm 1$ T at 2 K	202
Figure 5.12	Resistivity plot for CuFeAs in the temperature range 2 – 300 K	203
Figure 5.13	Neutron powder diffraction pattern of CuFeAs ($\lambda = 2.44$ Å). Arrows indicate the nuclear peaks from the aluminum sample holder. Bottom plot is the difference in diffraction intensities	204

collected at 2.5 K and 20 K.

- Figure 5.14** Temperature dependent magnetization in ZFC and FC conditions in the temperature range of 50-400 K for CuFeSb **205**
- Figure 5.15** Isothermal magnetization curves for CuFeSb at different temperatures (2, 300 and 380 K). Inset show the expanded M–H curves **206**
- Figure 5.16** ^{57}Fe Mössbauer spectrum of CuFeAs at different temperatures. **207**
- Figure 5.17** Order parameter plot of internal field (B) versus temperature for CuFeAs **208**
- Figure 5.18** Magnetic field dependent ^{57}Fe Mössbauer spectrum of CuFeAs at 2 K **210**
- Figure 5.19** ^{57}Fe Mössbauer spectra of CuFeSb at various temperatures **211**
- Figure 5.20** Order parameter plot between Hyperfine field B_{hyp} and temperature. **213**
- Figure 6.1** Crystal structure of LnCuAs_2 (Ln = Ce–Nd, Sm–Lu) in comparison with LaFeAsO structure. **222**
- Figure 6.2** Powder X–ray diffraction pattern of LnCuAs_2 (Ln = Pr, Nd, Tb, Dy, Ho and Yb). **225**

- Figure 6.3** Variation of lattice parameter (main panel) and unit cell volume (inset) with Ln-ions in LnCuAs_2 with rare-earth 227
- Figure 6.4** Susceptibility and its inverse plotted against temperature for LnCuAs_2 (Pr, Nd, Tb, Ho and Yb) 229
- Figure 6.5** T_N values for LnCuAs_2 compounds as obtained in our studies (circle), as reported in ref [2] (squares) and from de Gennes scaling (triangle). Susceptibility for Sm compound is not shown in figure 6.5 230
- Figure 6.6** Neutron powder diffraction of PrCuAs_2 at $T = 0.4$ K (black squares) and 10 K (blue circles). The solid (red) lines are the Rietveld fit results. The data at $T = 0.4$ K are vertically offset by 800. The inset shows the magnetic diffraction pattern by subtracting the data between 0.4 K and 10 K 231
- Figure 6.7** Illustration of irreducible representations (IRs) of LnCuAs_2 (only Ln ions are shown) with $\mathbf{K} = (0, 0, 0.5)$ as (a) Γ^1_2 , (b) Γ^1_3 , (c) Γ^2_9 , (d) Γ^2_{10} . 234
- Figure 6.8** Temperature dependence of the integrated intensity of the $\mathbf{Q} = (1, 0, 0.5)$ magnetic Bragg peak ($2\theta \approx 35.0$). The data collected above 10 K are used as background. The solid line is a mean field order parameter fit. The vertical dashed line indicates the 235

magnetic phase transition at $T_N = 6.4(2)$ K. Vertical bars represent standard deviation for each data point

Figure 6.9 (a) Neutron powder diffraction patterns of NdCuAs₂ at T = 0.4 K (green squares) and 10 K (blue circles). The solid (red) lines are the results of Rietveld fit. The T = 0.4 K data are vertically offset by 800, (b) and (c) show the magnetic diffraction pattern by subtracting the data between 0.4 K and 10 K for Nd and Dy respectively **236**

Figure 6.10 Temperature dependence of (0, 0, 1.5) magnetic Bragg intensity for the NdCuAs₂ (a) and DyCuAs₂ (b) respectively. Solid lines show the mean field order parameter fit results. The vertical dashed lines indicate the magnetic phase transition $T_N = 3.54$ and 10.1(2) K for the Nd and Dy sample, respectively **238**

Figure 6.11 (a) Neutron powder diffraction patterns of TbCuAs₂ at T = 2.5 K (green squares) and 40 K (blue circles) and (b) temperature dependent intensity of the two magnetic Bragg peaks for TbCuAs₂. The solid lines show the mean field order parameter fit and the vertical dashed lines indicate the magnetic phase transition temperature, $T_N = 9.44(5)$ K **239**

Figure 6.12 (a) Neutron powder diffraction pattern of HoCuAs₂ measured at T = 2 K (blue circle) and 40 K (green square). Inset shows the **240**

intensity difference between the two temperatures where only magnetic Bragg peaks are present and **(b)** temperature dependence of the magnetic Bragg peak intensities at $2\theta = 20.5^\circ$ (blue circle) and 6.7° (red square) of HoCuAs_2 . The vertical red dash line indicates the magnetic phase transition at $T = 4.41(2)$ K. The solid green line is a mean field order parameter fit. The inset of **(b)** show the evolution of the magnetic Bragg peak intensity as function of temperature and scattering angles in small scattering angle regime.

Figure 6.13 **(a)** Powder neutron diffraction pattern at 1.5 K (blue circles, 242 vertically offset by 800) and 20 K (green circles) for YbCuAs_2 . The red line shows the intensity difference between 1.5 K and 20 K and **(b)** Plot of low temperature susceptibility and its inverse measured at an applied external magnetic field of 500 Oe in ZFC condition. The peak in susceptibility at 4 K indicates magnetic phase transition.

LIST OF TABLES

Table No.	Table Caption	Page No.
Table 1.1	Value of T_c and upper critical field for some type II superconductors.	12
Table 1.2	Crystallographic parameters for LaOFeAs	18
Table 1.3	Structural parameters for high and low temperature phase of PbO type FeSe	21
Table 1.4	Atomic parameters of LiFeAs obtained from neutron powder diffraction studies at room temperature with lattice parameter $a = 3.776360 \text{ \AA}$, $c = 6.35679 \text{ \AA}$; space group $P4/nmm$	23
Table 1.5	Atomic parameters for $\text{LaO}_{0.5}\text{F}_{0.5}\text{BiS}_2$ (space group $P4/nmm$) with lattice parameters $a = 4.0527 \text{ \AA}$, $c = 13.3237 \text{ \AA}$	25
Table 1.6	A comparison between X-ray and neutron diffraction technique.	49
Table 2.1	Rietveld refined structural data for polycrystalline $\text{SmO}_{0.5}\text{F}_{0.5}\text{BiS}_2$ sample; Space group $P4/nmm$, $a = 4.0180(1) \text{ \AA}$ and $c = 13.529(4) \text{ \AA}$.	79
Table 2.2	Some single crystal data and structural refinement parameters for $\text{SmO}_{0.5}\text{F}_{0.5}\text{BiS}_2$.	80

Table 2.3	Atomic coordinates, Wyckoff positions, and isotropic equivalent displacement parameters for $\text{SmO}_{0.5}\text{F}_{0.5}\text{BiS}_2$ single crystal.	81
Table 2.4	Structural parameters for $\text{La}_{1-y}\text{Sm}_y\text{O}_{0.5}\text{F}_{0.5}\text{BiS}_2$ obtained after Rietveld refinement.	84
Table 3.1	Refined Lattice parameters and cell volume for $\text{Sr}_{0.5}\text{Ce}_{0.5}\text{FBiS}_{2-x}\text{Se}_x$ ($x = 0, 0.5$ and 1.0). Numbers in the parenthesis denote the estimated standard deviations in the last digit.	120
Table 3.2	Cell parameters and unit cell volume for $\text{Eu}_{1-x}\text{La}_x\text{FBiS}_2$.	122
Table 3.3	Refined crystallographic parameters for $\text{Eu}_{0.5}\text{La}_{0.5}\text{FBiS}_2$ at $T = 300$ K. Space Group $P4/nmm$; $a = 4.0744(1)$ Å, $c = 13.3366(7)$.	124
Table 3.4	Room temperature resistivity ($\rho_{300\text{K}}$), residual resistivity ratio (RRR), T_c and upper critical field ($H_{c2}(0)$) for $\text{Sr}_{0.5}\text{Ce}_{0.5}\text{FBiS}_{2-x}\text{Se}_x$ compositions.	126
Table 3.5	Weiss constant, Curie temperature, magnetic moment and T_c obtained for $\text{Sr}_{0.5}\text{Ce}_{0.5}\text{FBiS}_{2-x}\text{Se}_x$.	132
Table 3.6	Comparison of Debye temperature (θ_D) and Sommerfeld coefficient (γ) of some known Bi–S based superconductors and $\text{Sr}_{0.5}\text{Ce}_{0.5}\text{FBiS}_{1.5}\text{Se}_{0.5}$	138

Table 4.1	Ratio of Te:Se as estimated from the SEM–EDAX analysis for $\text{FeTe}_{0.5}\text{Se}_{0.5-x}\text{O}_x$. Amount of oxygen was calculated by subtracting obtained Se content from 0.5.	161
Table 4.2	Structural parameters for $\text{FeTe}_{0.5}\text{Se}_{0.5-x}\text{O}_x$ ($x = 0.0, 0.04$ and 0.06).	163
Table 4.3	Lattice parameters a and c for $\text{Fe}_{1-x}\text{Mn}_x\text{Te}_{0.5}\text{Se}_{0.5}$ ($x = 0, 0.01, 0.02$).	165
Table 4.4	Refined structural parameters for $\text{Fe}_{0.98}\text{Mn}_{0.2}\text{Te}_{0.5}\text{Se}_{0.5}$ obtained after keeping Mn at the two possible sites.	168
Table 5.1	Lattice parameter a and c for CuFeAs phases obtained through several reactions at different temperatures.	190
Table 5.2	Elemental ratio obtained from EDX analysis of CuFeAs sample at different regions.	191
Table 5.3	Refined structural parameters obtained after Rietveld refinement of PXRD data for CuFeAs with space group $P4/nmm$; $a = 3.7442(2)$ Å; $c = 5.8925(4)$ Å.	193
Table 5.4	Rietveld refinement results of powder neutron diffraction data of CuFeAs collected at 20 K: Space group $P4/nmm$; $a = 3.7348(4)$ Å, $c = 5.8452(7)$ Å	197

Table 5.5	Unidentified impurity Bragg peak positions and d -spacings.	197
Table 5.6	Refined structural parameters obtained for CuFeSb at 300 K: Space group; $P4/nmm$, $a = 3.9117(3)$ Å; $c = 6.2619(4)$ Å.	200
Table 5.7	Isomer shift (δ) and experimental line width (Γ) in the Mossbauer signal of CuFeAs with respect to temperature.	209
Table 5.8	Isomer shift (δ) and experimental line width (Γ) for CuFeSb with respect to temperature.	213
Table 6.1	Lattice parameters of all the LnCuAs ₂ phases calculated from X-ray diffraction data. Reported values is taken form reference	226
Table 6.2	Structure refinement results of neutron diffraction data for LnCuAs ₂ collected above T_N	228
Table 6.3	Basis vectors (BVs) for the space group $P4/nmm$ (#129) with k = (0, 0, 0.5). The decomposition of the magnetic representation for the R (R = Pr, Nd, Dy) site is $\Gamma^{\text{Mag}} = \Gamma^1_2 + \Gamma^1_3 + \Gamma^2_9 + \Gamma^2_{10}$. The atoms of the non primitive basis are defined according to 1: (0.25, 0.25, 0.246), 2: (0.75, 0.75, 0.754).	233

ABBREVIATIONS AND SYMBOLS

Å	Angstrom
°C	Centigrade
µm	Micrometer
Cm	centimeter
h	Hours
PXRD	Powder X-ray diffraction
TEM	Transmission Electron Microscopy
SEM	Scanning Electron Microscopy
EDX	Energy Dispersive X-ray Analysis
RRR	Residual resistivity ratio
µ	Magnetic Moment
H	Magnetic Field
µ _B	Bohr–magneton
eV	Electron – Volt
K	Kelvin
°	Degree (angle)
λ	Wavelength
Ω	Ohm
T	Tesla
G	Gauss
Oe	Oersted
M	DC Magnetization

χ_M	Molar Magnetic susceptibility (dc)
χ_M^{-1}	Inverse Molar Magnetic susceptibility (dc)
ρ	Resistivity
γ	Sommerfeld coefficient
θ	Weiss constant and Bragg's diffraction angle
θ_D	Debye temperature
k	Propagation vector
GPa	Gega Pascals
V	Electric field gradient
δ	Isomer shift
Γ	Line width